

# Numerical simulation of the internal plasma dynamics of post-flare loops

Fernández, C.A., [ultritas@yahoo.com.ar](mailto:ultritas@yahoo.com.ar)

*Facultad de Ciencias Exactas, Físicas y Naturales (UNC-Universidad Nacional de Córdoba, Argentina)*

Costa, A., [acosta@mail.oac.uncor.edu](mailto:acosta@mail.oac.uncor.edu)

*Instituto de Astronomía Teórica y Experimental (Córdoba, Argentina)  
Consejo Nacional de Investigaciones Científicas y Técnicas (CONICET)  
Facultad de Ciencias Exactas, Físicas y Naturales (UNC)*

Elaskar, S., [selaskar@yahoo.com](mailto:selaskar@yahoo.com)

*Facultad de Ciencias Exactas, Físicas y Naturales (UNC) and CONICET*

Schulz, W., [wschulz@efn.uncor.edu](mailto:wschulz@efn.uncor.edu)

*Facultad de Ciencias Exactas, Físicas y Naturales (UNC)*

We integrate the MHD ideal equations of a slender flux tube to simulate the internal plasma dynamics of coronal post-flare loops. We study the onset and evolution of the internal plasma instability to compare with observations and to gain insight into physical processes and characteristic parameters associated with flaring events. The numerical approach uses a finite-volume Harten-Yee TVD scheme to integrate the  $1D\frac{1}{2}$  MHD equations specially designed to capture supersonic flow discontinuities. We could reproduce the observational sliding down and upwardly propagating of brightening features along magnetic threads of an event occurred on October 1st, 2001. We show that high-speed downflow perturbations, usually interpreted as slow magnetoacoustic waves, could be better interpreted as slow magnetoacoustic shock waves. This result was obtained considering adiabaticity in the energy balance equation. However, a time-dependent forcing from the basis is needed to reproduce the reiteration of the event which resembles observational patterns -commonly known as quasi-periodic pulsations (QPPs)- which are related with large scale characteristic longitudes of coherence. This result reinforces the interpretation that the QPPs are a response to the pulsational flaring activity.

## I. INTRODUCTION

Oscillatory processes of several minutes periods in stellar coronae are associated with large scale quasi-periodic pulsations (QPPs) in flares. They were identified in X-ray stellar coronal flares (Mitra-Kraev et al. 2005) and were later reported for the Sun by Foullon et al. [2005]. Shorter period QPPs in the radio band are known since the early 70's (Aschwanden 2004). Also, systematic intensity perturbations in post-flare loops could indicate that they are the result of evaporation/condensation, or rising/falling plasma flow cycles, caused by the efficient heating of the flaring plasma from the chromosphere (De Groof et al. 2004). This suggests that energy released by flaring pulsations can induce oscillatory loop trapped processes. Many clear quasi-periodic phenomenon are believed to be associated with wave responses after chromospheric evaporation has taken place as the main initial matter inflow source for flare loops (Nakariakov et al. 2004). Recently, Sigalotti et al. [2009] simulated the propagation and damping of localized impulsive perturbations in coronal loops considering different dissipative mechanisms in the linear limit. As the authors state there is still no consensus over the actual mechanisms from which the waves originate. Moreover, the importance of different damping mechanisms is not fully understood due to the fact that different theoretical scenarios can describe similar observational frames. In this paper we confine to the ideal MHD approach -allowing the consideration of nonlinear waves and shocks which give rise to initially non-dissipative damping mechanisms- to evaluate its capability to adjust observational scenarios.

In Borgazzi and Costa [2005] we could describe an observational framework of catastrophic evacuation or high-speed descending flow picture resembling other authors results e.g. Kjeldseth-Moe and Brekke [1998]; Schrijver [2001]. An upwardly propagating pattern was also registered associated to other parts of the loop system. Also, the frequent recurrence of longitudinal compressible oscillations (e.g. in Borgazzi and Costa [2005], a quasi-periodic iteration of the event occurred 3 times in 1 h) were proposed to be associated with either large wavelength slow magnetoacoustic waves or limit-cycle solutions. In Costa and González [2006] we founded that limit cycle solutions associated with flow-based models are convergent with large wavelength wave-based models. Magnetoacoustic modes having wavelength of the order of the loop structure describe a basic oscillation between the kinetic energy of the parallel plasma flows and the internal energy i.e. the thermal perturbation. The structure of the obtained mode is such that in half of the period

the disturbance is always positive and the plasma emerges from the chromosphere while in the other half the plasma is negative and descending from the corona to the chromosphere.

In observational scenarios the dynamics is complex making it difficult to isolate the erratic flaring from the oscillations. Thus, due to the simplifications that are assumed for simulating physical quantities, the theoretical descriptions generally enables us to distinguish the behaviour of these components. Due to the high Reynolds number of the corona it could be expected that a perturbation could give rise to a slow magnetoacoustic wave or a rising/falling mechanism that iterates before it decays in a non-dissipative way.

Our intention is to provide a more accurate description of flaring multi-loop systems which exhibit a combined behaviour, sliding down and upwardly propagating appearance, to analyze the plasma dynamics interior to the loops and its relation with the flaring event, i.e. whether the oscillatory patterns -which could be associated with MHD waves and/or limit-cycle flow solutions in coronal structures- could be associated to internal or external driving mechanisms. As internal mechanism we refer to the development of non-dissipative second standing acoustic modes believed to be responsible for the induction of QPPs. These QPPs can be understood in terms of acoustic auto-oscillations, similar to the auto-oscillations in an electric-circuit generator (Tsiklauri et al. 2004). The other alternative implies that the QPPs are the resulting features of the external forcing produced by the flaring event.

## II. NUMERICAL METHOD

The basic MHD equations, the conservation of mass, conservation of momentum, energy balance, the magnetic induction equation together with a state equation, written in the so called conservative form result an hyperbolic-parabolic system of equations. The hyperbolic terms represent the convective effects and the parabolic ones the diffusive parts. These last terms are not considered in this paper so we work with an ideal MHD hyperbolic system of equations. We developed a 1D  $\frac{1}{2}$  numerical technique that consists of an approximate Riemann solver that allows to evaluate the variables inside each cell by means of the variation of the flows through the contour of the cell. The software that implements this numerical technique, has proven to be robust solving very demanding benchmarks such as magnetohydrodynamic Riemann problems and Hartmann flows. The MHD Riemann problem solutions are compressible non-steady flows; the Hartmann flows are incompressible and steady-state flows (Elaskar, et al. 2006a; 2006b; Maglione et al. 2007). Thus, the technique is seen as a reliable computational tool for the description of MHD flows.

Due to its accurate performance we apply the Harteen-Yee TVD technique (Total Variation Diminishing) which is specially designed to capture discontinuities when dealing with supersonic flows and to achieve a second order approach where the solution is smooth (Yee et al. 1985). Thus, the one non-dimensional equations considering non-stationary flow and written in conservative form are expressed as:

$$\mathbf{U}_t + \mathbf{F}(\mathbf{U})_x = 0 \quad (1)$$

where  $\mathbf{U}$  is the state vector of variables

$$\mathbf{U} = (\rho, \rho u_x, \rho u_y, \rho u_z, B_x, B_y, B_z, e)^T \quad (2)$$

and the hyperbolic fluxes are

$$\mathbf{F} = \left( \rho u_x, \rho u_x^2 - B_x^2 + p + \frac{1}{2} B^2, \rho u_x u_y - B_x B_y, \rho u_x u_z - B_x B_z, 0, \right. \\ \left. u_x B_y - u_y B_x, u_x B_z - u_z B_x, (e + p + \frac{1}{2} B^2) u_x - \mathbf{B} \cdot \mathbf{u} B_x \right)^T \quad (3)$$

$\rho$  indicates de density;  $u_x$ ,  $u_y$  and  $u_z$  are the velocity components;  $B_x$ ,  $B_y$  and  $B_z$  represent the components of the magnetic field vector;  $p$  is the pressure and  $B^2 = B_x^2 + B_y^2 + B_z^2$ . The total non-dimensional energy is

$$e = \frac{p}{\gamma - 1} + \frac{1}{2} \rho (u_x^2 + u_y^2 + u_z^2) + \frac{1}{2} \rho (B_x^2 + B_y^2 + B_z^2) \quad (4)$$

where  $\gamma$  is the ratio of specific heats.

In a quasi-linear form equation 1 results

$$\mathbf{U}_t + \mathbf{A}_c \cdot \mathbf{U}_x = 0 \quad (5)$$

where  $\mathbf{A}_c$  represents the matrix associated with the Jacobian fluxes, letter ‘c’ indicates that the derivation is with respect to the conservative state variables. A simpler form of the Jacobian fluxes is obtain as a function of the primitive variables

$$\mathbf{W} = (\rho, u_x, u_y, u_z, B_x, B_y, B_z, p)^T \quad (6)$$

Equation 5 in primitive variables reads

$$\mathbf{W}_t + \mathbf{A}_p \cdot \mathbf{W}_x = 0 \quad (7)$$

with the transformation rule

$$\mathbf{A}_p = \mathbf{W}_t + \mathbf{A}_c \cdot \mathbf{W}_x \quad (8)$$

The conservative form (eq. 5) is generally used for numerical purposes. They are appropriate to obtain accurate jump conditions at discontinuities and shocks (Leveque 2004) and they ensure that mass, momentum and energy are conserved. However, the eigenvalue and eigenvector manipulation is simpler in the primitive form (eq. 7), thus we solve the MHD equations using the conservative form and the eigenvectors are evaluated by means of the primitive formulation.

The resulting Jacobian flux has a null eigenvalue implying that is not possible to use a Riemann solver and thus an alternative Jacobian flux must be implemented. We used a technique developed by Powell [1995] and we obtained the primitive eigenvalues which resulted

$$\lambda_e = u_x; \quad \lambda_a = u_x c_a; \quad \lambda_f = u_x c_f; \quad \lambda_s = u_x c_s; \quad \lambda_d = u_x$$

where  $e$  stands for entropic,  $a$  for Alfvén, and  $s$  and  $f$  for slow and fast respectively. The Alfvén speed and the fast and slow speeds are respectively

$$c_a = \frac{B_n}{\sqrt{\rho}}; \quad c_{f,s}^2 = \frac{1}{2} \left( \frac{\gamma p + B^2}{\rho} \pm \sqrt{\left( \frac{\gamma p + B^2}{\rho} \right)^2 - \frac{\gamma p B_x^2}{\rho^2}} \right)$$

We normalized the eigenvectors following the proposal of Zachary et al. [1994] to avoid vector degenerations.

The explicit TVD scheme can be written as

$$U_{ij}^{n+1} = U_{ij}^n - \frac{\Delta t}{\Delta x} \left( \langle F_{i+\frac{1}{2};j}^n \rangle - \langle F_{i-\frac{1}{2};j}^n \rangle \right) \quad (9)$$

where the functions that determines the numerical fluxes are defined as

$$\langle F_{i+\frac{1}{2};j}^n \rangle = \frac{1}{2} \left( F_{i+1}^n + F_i^n + \left[ \sum_m \mathbf{R}_{i+\frac{1}{2}}^m \Phi_{i+\frac{1}{2}}^m \right]^{(n)} \right) \quad (10)$$

$\mathbf{R}$  is the matrix formed by the right eigenvectors of  $\mathbf{A}_c$ . The dissipation function is expressed as

$$\Phi_{i+\frac{1}{2}}^m = (g_{i+1}^m + g_i^m) - \sigma(\lambda_{i+\frac{1}{2}}^m + \gamma_{i+\frac{1}{2}}^m) \alpha_{i+\frac{1}{2}}^m \quad (11)$$

We also used a ‘‘limiter’’ function appropiated to optimize the one-dimensional flow (Elaskar et al. [2000]; Maglione et al [2003]).

$$g_i^m = \text{sgn}(\lambda_{i+\frac{1}{2}}^m) \max \left( 0, \min(\sigma_{i+\frac{1}{2}}^m | \alpha_{i-\frac{1}{2}}^m |, \sigma_{i-\frac{1}{2}}^m \frac{\text{sgn}(\lambda_{i+\frac{1}{2}}^m)}{2} \alpha_{i-\frac{1}{2}}^m) \right) \quad (12)$$

with  $\sigma(z) = |z| \rightarrow |z| \geq \varepsilon$  and  $\frac{1}{2\varepsilon}(z^2 + \varepsilon^2) < \varepsilon$ ;  $\frac{1}{\alpha_{i+\frac{1}{2}}^m}(g_{i+1}^m - g_i^m)$  if  $\alpha_{i+\frac{1}{2}}^m \neq 0$  and 0 if  $\alpha_{i+\frac{1}{2}}^m = 0$ .

The calculation process becomes simpler using the primitive variables to obtain

$$\alpha^m = L_p^m \cdot (W_{i+1} - W_i) \quad (13)$$

$L_p^m$  is the left eigenvector of matrix  $\mathbf{A}_p$  associated with wave  $m$ .

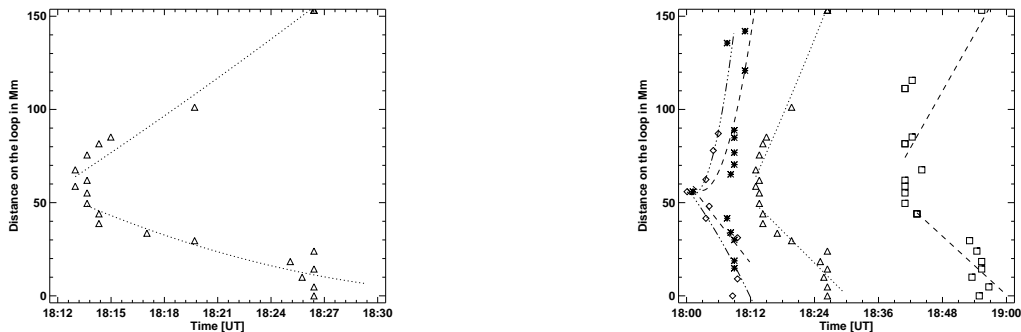


FIG. 1: a) TRACE location of the brightening, measured along the loop, as a function of time. The spatial origin is chosen at the loop’s Northern leg. b) Superposition of different events: locations of the brightenings as a function of time measured along a TRACE loop image: \* for the first TRACE sub-interval;  $\triangle$  for the second TRACE sub-interval and  $\square$  for the third TRACE sub-interval. To compare the two telescope results the MICA curve was superposed ( $\diamond$ ) on the TRACE first case. The different lines of each time sub-interval are the asymptotic curve values.

### III. THE PROBLEM

In Borgazzi and Costa [2005] we studied a post-flare event occurred October 1st, 2001 which was imaged by both, TRACE space telescope (Transition Region and Coronal Explorer, Handy et al. 1999) and MICA land telescope (Mirror Coronagraph for Argentina, Stenborg et al. 1999). We described an observational framework of catastrophic evacuation or high-speed descending perturbations which resembles QPPs as it was repeated 3 times in 1 h. An upwardly propagating pattern was also registered associated to other parts of the loop system. Different hypothesis are given in literature to justify why alternatively upward or downward evolving features are not seen (see the discussion in Borgazzi and Costa, 2005 and references therein). Figure 1a shows the location of brightening as a function of time measured over a virtual axis that extends along a whole complex loop i.e. a compound system of neighboring coronal isolated threads which exhibit a coherent behaviour. The origin of the axis was taken at the loop’s Northern foot and the distance was measured along the loop, considering that due to the location of the loop system and to the rough accuracy of the method projection effects could be discarded. The figure shows the sliding down of brightening features from the apex or bifurcation point towards both legs of the loop. Figure 1b shows the superposition of events occurred in the same loop system at different sub-intervals of time. The coherence is due to the fact that the figure represents the spatial and time behaviour of several apparently isolated tubes. Moreover, as we found that there was a time correlation between relative maxima when comparing different structures of the same active region we suggested that the large longitude chromospheric coherence founded i.e.  $\sim 300 Mm$ , must be associated with the forcing from the basis of the whole active region due to the intermittent flaring. However, this is not conclusive, recently Nakariakov et al. [2006] developed a model that shows that QPPs observed in a flaring loop can be triggered by MHD oscillations in another loop situated nearby, not necessarily magnetically linked with the flaring one, and thus giving another possible explanation for the coupling of oscillations in an active region.

Solar coronal conditions with large Reynolds numbers are well fitted by ideal MHD plasma models (i.e. infinite electrical conductivity  $\sigma \gg 1$  leading to vanishing viscosity and ohmic dissipation). We assumed that sources and sinks compensate each other, so the adiabatic energy equation holds, to investigate if the reiteration of features (Figure 1b) can be associated with the internal dynamics of the plasma, i.e., the second spatial harmonic of the acoustic mode which is believed to be responsible for QPP associated with flaring events (Tsiklauri et al. 2004). These undamped long wavelength solutions can be also thought of as limit cycles. These are nearly longitudinal magnetoacoustic modes that describe a basic oscillation between parallel plasma kinetic energy and plasma internal energy with a characteristic length of  $L/4$ ,  $L$  the length of the loop resulting in the balance between radiative losses and thermal conductive flux (Costa and González 2006). Otherwise, the reiteration of features could be associated to an external forcing from the chromospheric basis. This solution is generally suggested by the chromospheric coherence observed in the dynamics of many coronal events (e.g. Borgazzi and Costa 2005; Martínez et al. 2009). Of course, this description is not able to reproduce limit cycle models of the type proposed by Kuin and Martens [1982] which are associated with the generation and absorption of heat in open loop systems, neither the model proposed by Muller et al. [2004] via the assumption of different radiative loss functions, not taken into account here.

Firstly our intention is to reproduce an individual observational scheme. And secondly we investigate if the reiteration of features could be explained by an internal triggered mechanisms or if it requires an external forcing one. In the frame of this model the role played by the magnetic field is mostly to guide the plasma flow, so the simulations

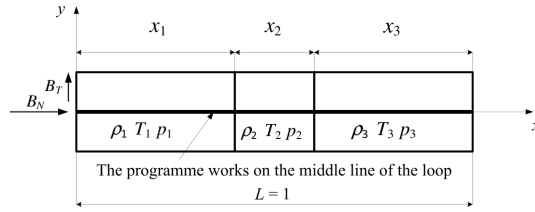
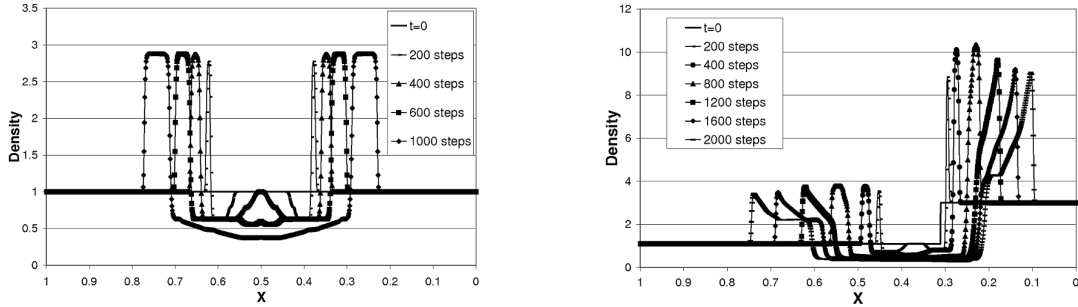


FIG. 2: Scheme of the loop description.

FIG. 3: Non-dimensional density -with respect to the background value- as a function of the non-dimensional loop length for different time steps. a) symmetric case, b) asymmetric case. The reference density and longitude values are  $\rho_o = 10^{11} cm^{-3}$  and  $L_o = 150 Mm$  respectively.

are performed varying the thermodynamical quantities of the loop in appropriate coronal and chromospheric ranges.

## IV. RESULTS AND DISCUSION

### A. Simulation of an individual sliding down event

We represent the loop system as a straight slender flux tube divided into three sections  $(x_1, x_2, x_3)$ ,  $x_1 + x_2 + x_3 = 1$  to integrate the non-dimensional 1D  $\frac{1}{2}$  MHD ideal equations. The non-dimensional component of the magnetic field along the loop is  $B_x = 1$ ;  $B_y = 0.01$ , is an initial transverse perturbation, note that  $B_x \gg B_y$ ; the reference magnetic field value used is  $B_o = 20 G$ . The non-dimensional variables are taken with respect to the second section

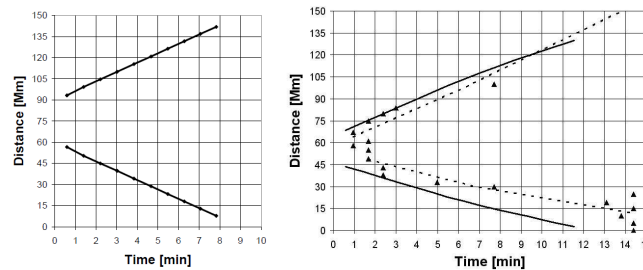


FIG. 4: Simulation of the individual a) symmetric case and b) the asymmetric case. The observational data are superimposed .Dot lines correspond to the asymptotic observational values in Figure 1a.

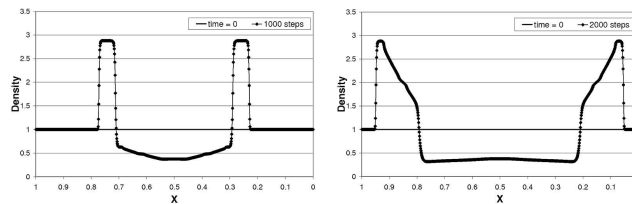


FIG. 5: Non-dimensional density as a function of the non-dimensional loop length (same reference values as in Figure 3) for: a) time step 1000 (3.84 min). Shock wave fronts  $x_{1s} = 0.2$ ;  $x_{2s} = 0.8$ , contact discontinuities  $x_{1c} = 0.3$ ;  $x_{2c} = 0.7$ , expansion waves  $x_{1e} = 0.45$ ;  $x_{2e} = 0.55$ ; b) time step 2000 (7.82 min). Shock wave  $x_{1s} = 0.05$ ;  $x_{2s} = 0.95$ , the expansion waves have interacted with the contact discontinuities and lowered the density and pressure.

values, e.g.  $v_1 = u_1/u_2$ . Several simulations for different sets of initial conditions were performed. The density values chosen are  $\rho_i = (10^9, 10^{10}, 10^{11}) \text{ cm}^{-3}$ , the reference density value used is  $\rho_o = 10^{11} \text{ cm}^{-3}$ ; the temperature values are  $T_i = (10^4, 10^5, 10^6, 2 \cdot 10^6, 10^7) \text{ K}$  with a reference value of  $T_o = (10^6 \text{ K})$ . The pressure is obtained from the ideal state equation. The reference longitude value is  $L_o = 150 Mm$ . For different combinations of the state values we obtain the correspondent evolutions. Figure 2 gives a scheme of the initial conditions.

### Symmetric case

We start with a symmetric partition to study the sensitivity of the system to the initial conditions, i.e.  $x_1 = 40\%L_o$ ,  $x_2 = 20\%L_o$ ,  $x_3 = 40\%L_o$ . Table I displays the six initial condition cases that adjusted the upper slope data of Figure 1a. They correspond to a temperature step initial condition of the unique non-dimensional case, i.e., all the cases in Table 1. We describe the spontaneous evolution of the system from this static initial condition; the initial speed value used is  $v_i = 0$ . Cases I and III can be associated with cold models and thus short loops. In the frame of this model, the fact that the case that adjust observations results from initial constant density reinforces the hypothesis of homogeneous density distribution of most loops. Figure 3a shows the evolution of the density front for different time steps. Figure 4a is obtained from Figure 3a assuming that the maximum of the perturbed density is a tracer of the observational features. We also obtain a resulting transverse magnetic field component smoothly modulated by the density front (the amplitude of the perturbed field is 10% of the non-perturbed one). However, following the classification by Nakariakov and Verwichte [2005] as the mode does not produce any noticeable perturbation of the loop minor radius it will be considered as a longitudinal mode, i.e., the magnetic field plays the role of being the wave guide of a fundamentally hydrodynamic shock.

A more detailed description can be obtained from Figure 5a-b and from the wave analysis provided by the numerical techniques used. The figure displays the time steps number 1000 (3.84 min or  $0.16 \tau_o$   $\tau_o$  is the acoustic transit time along half of the loop) and 2000 (7.82 min or  $0.32 \tau_o$ ) respectively. Time step 0 corresponds to  $\rho(0) = 1$ . Figure 5a shows two descendant shock wave fronts ( $x_{1s} = 0.2$ ;  $x_{2s} = 0.8$ ), two descendant contact discontinuities ( $x_{1c} = 0.3$ ;  $x_{2c} = 0.7$ ) and two descendant expansion waves ( $x_{1e} = 0.45$ ;  $x_{2e} = 0.55$ ). As the shock travels, the temperature, the density and magnetic field values are increased making the energy rise to values that could allow the observational detection. Note that the observation of moving brightening requires that these features must be time and spatially localized and thus, to make the detection possible, the density and temperature must be abruptly diminished again to compound a brightening feature. This effect is provided by the contact discontinuities which is recognized because the pressure and the velocity of the flow are not changed while the wave passes. The expansion waves are recognized because they diminish the density and pressure values. From the comparison of time step 1000 and time step 2000 (cases a and b of Figure 5), we see that the expansion wave has a larger speed than the contact discontinuity, i.e. when the expansion wave reaches the contact discontinuity the density and the pressure of the whole wave system is diminished. From Figure 3 we also note that the expansion waves have initially an ascendant phase (compare the density distribution at the loop center of steps 200 and 400 of the figure); the waves collide at the center and then travel downwards. Figure 5b shows for time step 2000 the position of the descendant shock fronts ( $x_{1s} = 0.05$ ;  $x_{2s} = 0.95$ ). Also, the expansion waves have interacted with the contact discontinuities and lowered the density and pressure leaving behind a coupled nonlinear system of waves, i.e., the features located at  $x_1 = 0.2$ ;  $x_2 = 0.8$  in Figure 5b can no longer be interpreted as contact discontinuities.

### Asymmetric case

To simulate the asymmetry in the location of the bifurcation point of Figure 1a-b we assume  $x_1 = 0.31$ ,  $x_2 = 0.12$ ,  $x_3 = 0.57$ , which is in correspondence with the asymmetrical dynamical geometry of the loop system, see Figure 1a. The aim is to reproduce the downward branch slopes of Figure 1a, taking into account that to make the signal detectable the maxima must be higher than the background intensity value, e.g. Figure 3b. Starting from the

non-dimensional symmetric case, the pressure and density of the segments  $x_i$  are changed to reproduce the slopes. The slopes result strongly sensitive to variations of the density, i.e., note from Figure 3b that higher background densities (right line starting at  $x = 0.3$ ) imply lower wave speeds (compare the speed of the right and left perturbations). We obtained few cases that could reproduce the conditions. The new non-dimensional initial condition values of segments  $(x_1, x_2, x_3)$  that adjusted the observations were  $\rho = (1.1, 1.1, 3)$  pressure  $p = (0.02, 1, 0.025)$  and  $T = (0.02, 1, 0.01)$ . Figure 4b is obtained in the same way than in the symmetric case, assuming that the maximum of the perturbed density is a tracer of the observational features. The observational curve is superimposed over the numerical one showing good accordance between them.

In the frame of this first model, it is not possible to give account for the reiteration of the brightening features of Figure 1b. As a consequence of the low density values produced by the pass of the expansion wave, the temperature and density acquire very low values in the back front which are not recovered in the ascending phase. In all cases, the evolution from initial values systematically show a deep vacuum at the back front, i.e., density and temperature diminish to almost 30% of the initial background values. This can also be seen from Figure 3, the center values are lowered below the background density. However, to investigate if the low density region could be narrowed we vary the  $x_i$  partition. In this case, we obtain that the slope of the curve remained the same as in Figure 4a and the vacuum region is narrowed but could not be lowered more than 8% of the total length, e.g., for  $x_2 = 2$  the low density region covers 8% of the center of the loop. Moreover, the fact that Figure 1b shows only descendant features and not ascendant ones could be associated with the instrumental resolution that provides a limit value to the detection of the density. This implies that the density associated with the brightening of all the observed descendant branches must be higher than the ascendant ones, and last ones presumably not detectable; this fact could not be reproduced by the numerical simulation of this model. In Costa et al. [2009] we show that the pass of this type of non-linear waves form a vacuum tail that can give account of the so-called tadpole phenomenon.

## B. Simulation of the external forcing from the bases

The different branch speeds of an individual phenomenon were adjusted changing the initial conditions, as in the first model approach given in subsection (4.1), but it was not possible to reproduce its iteration. To reproduce the sliding down features, as in Figure 1b we decided to investigate the second triggering mechanism proposed. This is the chromospheric forcing from the loop footpoints produced by a transient oscillation associated with individual flare burst. The possible forcing functions are limited by the fact that they must reproduce the speeds and cadences of Figure 1b. The temporally and spatially localized impulse deposition, resembling a mass injection in the bases of the loop, was switched off before the start of the simulation. Thus, the forcing must be considered as a boundary condition imposed to an homogeneous loop, i.e., with initial non-dimensional density  $\rho = (1, 1, 1)$  and temperature  $T = (0.1, 0.1, 0.1)$ . Figure 6a shows the density variation obtained assuming the action of one individual flare burst modeled by a forcing function  $f = A \sin^6(\omega t)$ , with  $A = 3$ , and the frequency  $\omega = 6.28$ , which corresponds to a deposition of energy of  $\sim 10^3 \text{ erg cm}^{-3}$  on a typical loop. The value  $\omega = 6.28$  represents a dimensional characteristic time of  $\tau = 9.3 \text{ min}$ . The  $x_i$  partition used is the same as in the first symmetric case.

All the descendant branches have larger values of the perturbed density than the ascendant ones. The difference varies between  $\sim 20\%$  and  $40\%$  (for the non-dimensional  $x$  value varying between 0.2 and 0.8) and thus, if the model is accurate, i.e., only the descendant branches are detected, an intensity threshold  $H$  can be numerically obtained. In fact, in the EUV and X-ray band, the emission intensity is modulated by the density perturbations as  $H \propto (\rho_0 + \delta\rho)^2$

$$H_A = (\rho_0 + \delta\rho)_A^2 < H < (\rho_0 + \delta\rho)_D^2 = H_D \quad (14)$$

and the threshold can be estimated by the above relation.  $\rho_0$  is the background density,  $\delta\rho$  the perturbed density,  $A$  and  $D$  means ascendant and descendant respectively. Taking into account the numerical results, i.e., non-dimensional densities  $(\rho_0 + \delta\rho)_A = 2.45$  and  $(\rho_0 + \delta\rho)_D = 1.7$ , we obtain a mean value of  $\langle H \rangle = 4.446 \cdot 10^{-22} \text{ cm}^{-6}$  with a  $\Delta H = 3.113 \cdot 10^{-22} \text{ cm}^{-6}$  and  $\Delta H / \langle H \rangle = 0.7001$ . Figure 6b is obtained from Figure 6a using the intensity threshold  $\sqrt{\langle H \rangle} = 2.11$  to resemble the observational features, i.e., with only descendant branches. The ascendant branches are more intense than the descendant ones, however, extended ascendant features ( $0 < x < 0.2$  and  $0.8 < x < 1$ ) can be distinguished at the location of chromospheric feet in Figure 6b. These features are correlated with the accumulation of observational points at the chromospheric footpoints in Figure 1b and could be indicating the wave front bouncing.

The dimensional speeds of the numerical descendant branches are:  $v_1 = 106 \text{ km sec}^{-1}$ ,  $v_2 = 87 \text{ km sec}^{-1}$ , and  $v_3 = 86 \text{ km sec}^{-1}$ , respectively. To compare with observation we take the mean value of the speeds of the northern and southern descendant branches of each event of Figure 1b. The mean observational speeds are:  $u_1 = 129 \text{ km sec}^{-1}$ ,  $u_2 = 82 \text{ km sec}^{-1}$ , and  $u_3 = 65 \text{ km sec}^{-1}$ , respectively. The time separations between branches for the numerical case are:  $T_{1,2} \sim 24 \text{ min}$ ,  $T_{2,3} \sim 28 \text{ min}$ , and  $T_{3,4} \sim 28 \text{ min}$  and the correspondent observational quantities (Figure 1b) are:  $T_{1,2} \sim 12 \text{ min}$ ,  $T_{2,3} \sim 26 \text{ min}$ , and  $T_{3,4} \sim 22 \text{ min}$ .

To compare the two model approaches, i.e., spontaneous and forced, we display the density profiles obtained for different fix temporal values of Figure 6:  $t = 2.23$ ,  $t = 2.57$  and  $t = 3.30$ . The resulting features are shown in Figure 7. The density profile at  $t = 2.23$  is shown in Figure 7a. We see two descending shock fronts at the center of the figure, i.e.,  $x_{1s} = 0.4$  and  $x_{2s} = 0.6$ , together with ascending waves corresponding to the rebound of the first shock. This last features have their maximum at  $x_1 \sim 0.1$  and  $x_2 \sim 0.9$  respectively and both are below the non-dimensional density threshold corresponding to  $\sqrt{H_{nd}} = \rho_H \sim 2.11$ . The density profile at  $t = 2.57$  is shown in Figure 7b. The two descending shocks are at  $x_{1s} \sim 0.2$  and  $x_{2s} \sim 0.8$ . At the center the nonlinear interaction of waves lowers the density. Only descendant shock features are detected due to the density threshold. The density profile at  $t = 3.30$  is shown in Figure 7c. Again, at the center the density is lowered due to the continue nonlinear interaction of waves. Only ascendant features from last rebound are detectable due to the density threshold  $\rho_H = 2.11$ . Figure 7b and Figure 5a have common sharp edges features indicating the presence of shock fronts. From Figure 7c and Figure 5b we see common regions formed by interaction of waves near the bases; the interaction of waves finish smoothing out the density profiles. The differences on the correspondent shapes are related with the differences in the triggering mechanisms (the spontaneous evolution vs. external forcing from the bases), however, the resulting cadences and characteristic speeds are the same as the observational ones.

Zaitsev and Stepanov [1989] introduced a model from where they derived relations between flare loop parameters as a function of loop length, period and amplitude of the oscillation:

$$\begin{aligned}
 T &\sim 1.2 \cdot 10^{-8} \frac{L^2}{\tau^2} \frac{\Delta H}{\langle H \rangle} [K] \\
 n_e &\sim 2.2 \cdot 10^{-10} \frac{L^3}{Q\tau^4} \left( \frac{\Delta H}{\langle H \rangle} \right)^{1.5} [cm^{-3}] \\
 B &\sim 6.7 \cdot 10^{-17} \frac{L^{2.5}}{\sqrt{Q}\tau^3} \left( \frac{\Delta H}{\langle H \rangle} \right)^{0.75} [G]
 \end{aligned} \tag{15}$$

where  $T$ ,  $n_e$ ,  $L$ ,  $B$  are the temperature, density, length and magnetic strength of the loop. If we take  $\tau = 9.3 \text{ min}$ , the dimensional characteristic time associated with the flare bursts;  $Q = 1$ , the quality factor or the number of individual flare bursts; and the intensity amplitude of the flare oscillating features as the numerical intensity amplitude,  $\Delta H/H$ , we can estimate the temperature, electron density and the magnetic field strength as

$$T \sim 6.3 \cdot 10^6 \text{ K}, \quad n_e \sim 4.9 \cdot 10^9 \text{ cm}^{-3}, \quad B \sim 8.7 \text{ G}.$$

To adjust the observations we performed several calculations varying the parameters  $\Delta H/\langle H \rangle$ ,  $Q$  and  $\tau$  respectively. We noted that the increasing of  $\Delta H/\langle H \rangle$ , corresponds to more pronounced curves of the descending branches and that more complex patterns can be obtained depending on  $Q$ , the number of individual flare burst chosen and the time distance between them,  $\tau$ . Taking into account the approximations we assumed and the numerical simplifications of the model we note that the values obtained are in good agreement with the observational values. The evaluation of the relative importance of the parameters and initial conditions to produce different patterns that could be compared to observations together with the consideration of nonideal contributions will be a matter of a new work.

A few words with respect to the consideration of diffusive terms in the equations must be added. Longitudinal modes can be affected by the thermodynamic properties of the medium. However, the fact that this type of modes is selectively seen in hot loops, where the mode damping is strongest, remains an open question. The scenario we are dealing with shows that nonlinear wave interaction processes are responsible of smoothing out sharp edges in a non-dissipative regime. This suggests that we are describing the stage where a non-dissipative transfer of energy from the large spatial scales to the small ones is predominantly at work before the small scales allow an efficient action of dissipation.

A novelty of this work is that it proposes that the description in terms of shock waves is more common than what it was supposed. Low  $\beta$  value media have larger values of the Alfvén speed than the sound speed. These two characteristic parameters of the coronal plasma determine the type of processes and energies associated to them that can be involved in its dynamics. The fact that in general, depending on the  $\beta$  value, the sound speed is the smallest one suggest that it must not be unusual that compressional perturbations reach shock wave speeds. Inhomogeneous features in the medium can easily couple the transverse alfvénic component with the longitudinal one and thus transfer energy to the acoustic mode allowing that hydrodynamic shock waves, guided by magnetic fields, can propagate.



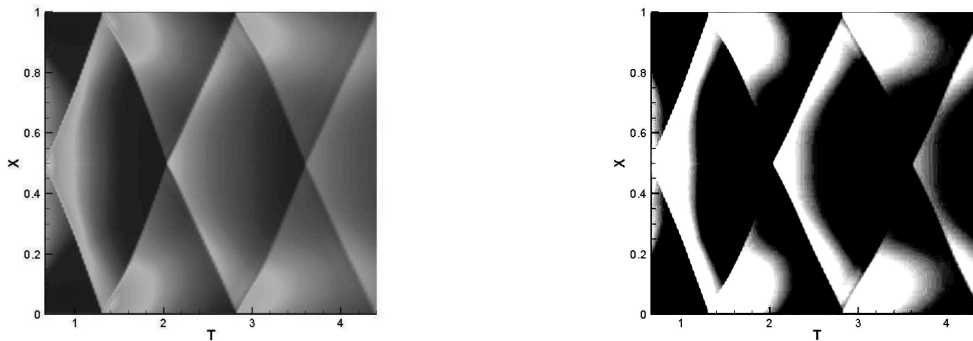


FIG. 6: a) Non-dimensional descendant and ascendant density features as a function of the non-dimensional time. b) Non-dimensional descendant density features using the threshold  $H$ .  $x = 1$  is equivalent to  $L = 150 Mm$ . One time division is equivalent to  $18 \text{ min } 10 \text{ sec}$ .

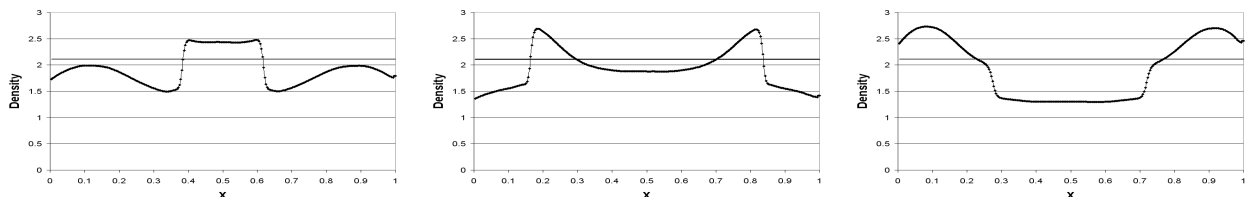


FIG. 7: Non-dimensional density as function of the non-dimensional loop length taken from the model in subsection (4.2) at the a) non-dimensional time 2.23, two descending shock fronts  $x_{1s} = 0.4; x_{2s} = 0.6$ ; ascending waves, corresponding to the rebound of the first shock fronts, with maxima at  $x_1 \sim 0.1; x_2 \sim 0.9$ , both below the threshold  $\rho_H \sim 2.11$ ; b) non-dimensional time 2.57, two descending shock fronts at  $x_{1s} \sim 0.2; x_{2s} \sim 0.8$ ; ascending waves lower the density at the center of the figure; c) non-dimensional time 3.30, the interaction of waves smooth the profile, only the ascendant features are detected due to the density threshold,  $\rho_H \sim 2.11$ .

## V. CONCLUSIONS

We have integrated the MHD ideal equations of a slender flux tube to simulate the internal plasma dynamics of coronal post-flare loops. We could reproduced the observational behaviour of brightening features along magnetic threads of an event occurred on October 1st, 2001, i.e., characteristic speeds and times. Our intention was to analyze the plasma dynamics interior to postflare loops and its relation with flaring events, i.e. whether the oscillatory patterns could be associated to internal or external driving mechanisms. This is, whether non-dissipative second standing acoustic modes could be responsible for the induction of QPPs or if they are resulting features of an external forcing produced by the flaring event. We showed that, in the frame of our model, to reproduce the iteration of sliding down observations a time-dependent forcing from the basis is required and thus the interpretation that the QPPs are responses to the pulsational flaring activity is reinforced.

We also found that high-speed downflow perturbations usually interpreted as slow magnetoacoustic waves can be better interpreted as slow magnetoacoustic shock waves.

Case	$\rho_1 = \rho_3 \text{ (cm}^{-3}\text{)}$	$\rho_2 \text{ (cm}^{-3}\text{)}$	$T_1 = T_3 \text{ (K)}$	$T_2 \text{ (K)}$	wave speed	sound speed
I	$10^{10}$	$10^{10}$	$10^4$	$10^5$	0.81	0.374
II	$10^{10}$	$10^{10}$	$10^5$	$10^6$	0.81	0.374
III	$10^{11}$	$10^{11}$	$10^4$	$10^5$	0.81	0.374
IV	$10^{11}$	$10^{11}$	$10^5$	$10^6$	0.81	0.374
V	$10^{10}$	$10^{10}$	$10^5$	$2.10^6$	0.771	0.265
VI	$10^{11}$	$10^{11}$	$10^5$	$2.10^6$	0.771	0.265

TABLE I: Values of the six initial condition cases that adjust the observational data of the symmetric case (see Figure 1a). The wave front speed and the acoustic speed were nondimensionalized with the Alfvén speed ( $v_A = 1$ ).

### Acknowledgments

We are grateful to Dr. Tamagno for his comments and suggestions that helped to improve the quality of the paper.

- 
- [2004] Aschwanden, M. J. “Physics of the Solar Corona” (Springer-Praxis), 2004
- [2005] Borgazzi, A., Costa, A., A&A 441, 327,2005
- [2006] Costa, A., González, R., A&A 458, 3, 953, 2006
- [2009] Costa, A., Elaskar, S., Fernández, C., Martínez, G., submitted to A&A, 2009
- [2004] De Groof, A., Berghmans, D., van Driel-Gesztelyi, L., Poedts, S., A&A 415, 1141, 2004
- [2000] Elaskar, S., Brito H., Tamango, J., Int. Astronautical Federation, Paper IAF-00-S.4.10,2000
- [2006] Elaskar, S., Brito H., Tamango, J., Int. Astronautical Federation, Paper IAC-06-C4.P.4.10, 2006
- [2006] Elaskar, S.; Falcinelli, O.; Maglione, L.; Tamagno, J.; Brito, H. and Schulz, W., International Symposium on Electrohydrodynamics Proceeding, ISEHD, 143, 2006
- [2005] Foullon,C., Verwichte,E. Nakariakov, V.M., A&A 440, L59, 2005
- [1999] Handy, B.N., Acton, L.W., Kankelborg, C.C., Solar Phys. 184, 229, 1999
- [1998] Kjeldseth-Moe, O. and Brekke, P., Solar Phy. 182, 73, 1998
- [1982] Kuin, N.P.M., Martens, P.C.H., A&A 108,L1, 1982
- [2004] Leveque, R. J. “Numerical Methods for Conservation Laws” (Verlag-Birkhuser), 1992
- [2009] Martínez, G., Costa, A., Rovira, M., in preparation, 2009
- [2003] Maglione, L., Elaskar, S., Brito, H., Paper: IEPC-03-070, 2003.
- [2007] Maglione, L., Elaskar, S., Brito, H., 1., H.; Dean, R., Lifschitz, L., PAMM, 1,7, 2007
- [2005] Mitra–Kraev, U., Harra, L.K., Williams, D.R., et al., A&A 436,1041, 2005
- [2004] Muller, D.A.N., Peter, H., Hansteen, V.H., A&A 424,289, 2004
- [2006] Nakariakov, V.M., Foullon, C., Verwichte, E., et al., A&A, 452,343, 2006
- [2004] Nakariakov, V.M., Tsiklauri, D., Kelly, A., Arber, T.D., Aschwanden, M.J., A&A 414, L25, 2004
- [2005] Nakariakov, V.M., Verwichte, E., Living Rev. Solar Phys.,2, 3, 2005
- [1995] Powell, K., NASA Contract No NAS1-19480, ICASE, NASA Langley Research Center, Hampton, 1995.
- [2001] Schrijver, C.J., Solar Phys. 198, 325, 2001
- [2009] Sigalotti, L. G., Guerra, J. A. Mendoza–Briceño C. A., Solar Phys. 254, 127, 2009
- [1999] Stenborg, G., Schwenn, R., Srivastava, N., Inhester, B., Podlipnik, B., Rovira, M., Francile, C., Space Sci. Rev. 87, 307, 1999
- [2004] Tsiklauri, D., Nakariakov, V.M., Arber, T.,D., Aschnaden, M.J., A&A 422, 351, 2004
- [2005] Verwichte, E., Nakariakov, V.M., Cooper, F.C., A&A 430, L65, 2005
- [1985] Yee, H., Warming, R. and Harten, A., J. Compu. Phy., 57, 327, 1985.
- [1989] Zaitsev, V.V., Stepanov, A.V., Sov.Astron.Lett., 15,66, 1989
- [1994] Zarachay, A.; Malagoli, A. and Collela, P., SIAM J Scientific Comp., 15, 263, 1994